



## Synergistic degradation of NO and C<sub>7</sub>H<sub>8</sub> for inhibition of O<sub>3</sub> generation

Kanglu Li <sup>a,b</sup>, Hong Wang <sup>a</sup>, Lvcun Chen <sup>a</sup>, Jieyuan Li <sup>a</sup>, Fan Dong <sup>a,\*</sup>

<sup>a</sup> Yangtze Delta Region Institute (Huzhou) & Institute of Fundamental and Frontier Sciences, University of Electronic Science and Technology of China, Huzhou 313000, China

<sup>b</sup> College of Architecture and Environment, Sichuan University, Chengdu 610065, China



### ARTICLE INFO

**Keywords:**  
Air purification  
VOCs  
NO<sub>x</sub>  
O<sub>3</sub> generation  
Synergistic control

### ABSTRACT

NO<sub>x</sub> and VOCs are primary air pollutants and their photochemical reactions would generate secondary pollutants like O<sub>3</sub> with NO<sub>2</sub> intermediate as the direct precursor. Here we apply a highly efficient In(OH)<sub>3</sub> photocatalyst to degrade mixed NO and C<sub>7</sub>H<sub>8</sub> for inhibition of photochemical O<sub>3</sub> generation. The dual pollutants show synergistic interaction from the adsorption process to photocatalytic reaction. C<sub>7</sub>H<sub>8</sub> and NO exhibit non-competitive adsorption and coupling reaction effects on In(OH)<sub>3</sub> surface. The coupling intermediate C<sub>7</sub>H<sub>8</sub>NOH would be oxidized to nitrotoluene and further decomposed into CO<sub>2</sub> and nitrates. Meanwhile, the protons and electrons released during the oxidation of C<sub>7</sub>H<sub>8</sub> can reduce NO to NH<sub>4</sub><sup>+</sup>. Gibbs free energy calculation reveals that the coupling and reduction reactions are more favorable than the oxidation of NO to NO<sub>2</sub>. The new conversion path of NO on In(OH)<sub>3</sub> when C<sub>7</sub>H<sub>8</sub> coexists could enable an increase of NO conversion efficiency to 100.0% and a decrease of NO<sub>2</sub> selectivity to only 3.7%, thus highly inhibiting the formation of O<sub>3</sub>.

### 1. Introduction

Nitrogen oxides (NO<sub>x</sub>) [1–3] and volatile organic compounds (VOCs) [4–6] are harmful primary pollutants, which would bring severe adverse effects to human health and ecological environment. Coexisting NO<sub>x</sub> and VOCs will also cause ozone (O<sub>3</sub>), fine inhalable particles (PM<sub>2.5</sub>), and other second pollution [7–9]. In China, air pollution control has gained appreciable effects so far. The concentration of PM<sub>2.5</sub> continues to decline, [10] but the O<sub>3</sub> pollution has shown a rapid rise [11]. The O<sub>3</sub> pollution has become one of the bottlenecks that restrict the improvement of air quality in China, as well as in other developing countries. O<sub>3</sub> can irritate the respiratory system, cause cardiovascular and nervous system diseases and damage the immune system. O<sub>3</sub> also has direct or indirect effects on vegetation ecology and global climate [12].

Generally, O<sub>3</sub> is produced from a series of photochemical reactions between NO<sub>x</sub> and VOCs when they coexist [13]. Simultaneous control of NO<sub>x</sub> and VOCs may lead to additional benefits in reducing O<sub>3</sub> emission [14,15]. Sunlight will trigger photochemical reactions and generate secondary pollution, but it is also a source of energy that can be utilized by photocatalyst [16–18]. Photocatalysis may turn predicament into power, change the reaction pathway between NO<sub>x</sub> and VOCs and synergistically convert them into small molecules (such as NO<sub>3</sub>, CO<sub>2</sub>, H<sub>2</sub>O) [19–21]. However, due to the complexity of the reaction processes and

the limitation of the analysis methods, most reports focus on degradation of only one single pollutant, which does not fulfill the actual scenarios with the coexistence of multiple pollutants. Unfortunately, few studies have considered the degradation of multiple pollutants, and the crucial issues include the interaction between pollutants, the generation of secondary pollutants, and the reaction pathway [22–25].

Indium hydroxide (In(OH)<sub>3</sub>) was found to be an efficient and stable photocatalyst in degrading aromatic VOCs [26]. Herein, In(OH)<sub>3</sub> is applied to degrade the mixture of two typical pollutants (NO and C<sub>7</sub>H<sub>8</sub>) and minimize the generation of O<sub>3</sub> simultaneously. The generation of O<sub>3</sub> is obvious under light irradiation when NO and C<sub>7</sub>H<sub>8</sub> coexist without photocatalyst. In contrast, In(OH)<sub>3</sub> photocatalyst shows a great performance for simultaneous control of NO, C<sub>7</sub>H<sub>8</sub> and O<sub>3</sub>. The mechanism has been investigated theoretically and experimentally. In situ DRIFTS and DFT calculation reveal the non-competitive adsorption and coupling reaction effects between the dual pollutants. GC-MS and IC identify the key intermediates and products. The introduction of C<sub>7</sub>H<sub>8</sub> can change the reaction pathway of NO oxidation and improve the conversion to NO<sub>3</sub><sup>-</sup> and NH<sub>4</sub><sup>+</sup>. Gibbs free energy calculation figures out that the oxidation reaction of NO to NO<sub>2</sub> (direct precursor for O<sub>3</sub> [27]) is less favorable than the coupling and reduction reactions of NO when C<sub>7</sub>H<sub>8</sub> coexists. The enhanced total conversion of NO<sub>x</sub> could cut off the formation path for O<sub>3</sub>. An overall conversion pathway is proposed to

\* Corresponding author.

E-mail addresses: [dfctbu@126.com](mailto:dfctbu@126.com), [dongfan@uestc.edu.cn](mailto:dongfan@uestc.edu.cn) (F. Dong).

illustrate the mechanism of synergistic control of multi pollutants. This work studies the synergistic degradation of mixed NO and VOC and the inhibition of photochemical O<sub>3</sub> generation by photocatalysis for the first time. The finding in this work is a significant step to the exploration of synergistic control of multi air pollutants, showing the special advantage of photocatalysis for utilizing solar energy to purify primary and secondary pollutants.

## 2. Experimental

### 2.1. Synthesis and characterization of photocatalyst

Indium (III) nitrate hydrate (In(NO<sub>3</sub>)<sub>3</sub>·xH<sub>2</sub>O, 99.99%) was purchased from Adamas, and ammonium hydroxide solution (NH<sub>4</sub>OH, 25–28%) was purchased from Greagent. The In(OH)<sub>3</sub> photocatalyst was prepared by a precipitation method. 5.0 ml NH<sub>4</sub>OH diluted with 10.0 ml deionized water was added dropwise into 0.1 M In(NO<sub>3</sub>)<sub>3</sub> aqueous solution until the pH reached around 8.5. After the mixture was aged for 2 h, the precipitate was washed six times and dried at 80 °C for 12 h. More details about the characterization of photocatalyst can be found in the [Supporting Information](#).

### 2.2. Pollutants degradation measurement

The photocatalytic degradation of NO and C<sub>7</sub>H<sub>8</sub> was measured using a continuous flow system at room temperature ([Fig. S1](#)). Four glass sheets supporting 0.2 g of photocatalyst evenly were placed in the reactor (200 mm × 100 mm × 17 m) and covered by a quartz glass lid. A 300 W UV mercury lamp with a filter ( $\lambda > 200$  nm) producing no ozone was placed above the reactor vertically as the light source. Four gas monitors simultaneously measure the concentrations of NO, C<sub>7</sub>H<sub>8</sub>, dry air and wet air, and the four streams are mixed in a chamber before the reactor. The concentrations of NO and C<sub>7</sub>H<sub>8</sub> were both controlled at 30 ppm to simulate the polluted situations like factory boundary, where the high concentration pollutants are pre-treated by traditional methods. The gas humidity was controlled at 50%, and the total flow rate was set to 1.0 L/min. The concentrations of NO, C<sub>7</sub>H<sub>8</sub>, H<sub>2</sub>O and CO<sub>2</sub> were continuously recorded by a multi-gas analyzer (DKG-42A, Duke Technology). The pollutant conversion efficiency was calculated as  $\eta$  (%) = (C<sub>0</sub> – C)/C<sub>0</sub> × 100%. C<sub>0</sub> and C depicted the concentration of NO or C<sub>7</sub>H<sub>8</sub> at the adsorption equilibrium and the real-time concentration in the outlet stream, respectively. The concentration of O<sub>3</sub> was measured by an ozone analyzer (106 L, 2B Model). The concentration of NO<sub>2</sub> was detected by a flue gas analyzer (350, Testo). The NO<sub>2</sub> selectivity was calculated as  $\omega$  (%) = (C(NO<sub>2</sub>) – C<sub>0</sub>(NO<sub>2</sub>))/(C(NO) – C<sub>0</sub>(NO)) × 100%.

### 2.3. Analytical methods

The adsorption and photocatalytic reaction processes were observed by the in situ diffuse reflectance infrared spectroscopy equipped with an in situ diffuse reflectance cell, a high-temperature reaction chamber, and a UV light source (in situ DRIFTS, Tensor II, Bruker). He was used to empty the residual gas at 100 °C after the sample was put in the cell. Once the pollutant was led into the cell, the real-time spectra were recorded every 2 min to investigate the change of surface species on photocatalyst.

The carbon-containing products in the outlet stream were collected with a sample tube and detected by the gas chromatography-mass spectrometry (GC-MS, GC-2030, GCMS-QP2020 NX, Shimadzu). All the products were identified via retention time by the NIST 17 database. The nitrogen-containing products adsorbed on photocatalyst were extracted with ultrapure water and distinguished by ion chromatography (IC, Essential, Shimadzu).

The microscopic adsorption and reaction processes were simulated by density functional theory (DFT) calculation using the plane-wave-based “Vienna ab initio simulation package” (VASP 5.4.1). The

interactions between atomic cores and electrons were described by the projector-augmented-wave method (PAW), and the electron exchange-correlation interaction was described by the Perdew-Burke-Ernzerhof generalized gradient approximation (PBE-GGA). A (2 × 2 × 2) supercell (containing 32 In, 96 O and 96 H atoms) with 15 Å vacuum thickness was used to model (200) facet of In(OH)<sub>3</sub> crystal ([Fig. S2](#)). The plane-wave cutoff energy was set to 400 eV and the k-point grid of 2 × 2 × 1 was adopted. The energy and the force convergence for geometry optimization were set to  $1 \times 10^{-4}$  eV and 0.02 eV/Å, respectively. The adsorption energy E<sub>ads</sub> = E<sub>tot</sub> – E<sub>slab</sub> – E<sub>molecule</sub>. The reaction energy E<sub>react</sub> = E<sub>final</sub> – E<sub>initial</sub>. The zero-point energy (ZPE) and entropy corrections were taken into account for free energies calculations,  $\Delta G = \Delta E_{DFT} + \Delta E_{ZPE} - T\Delta S$ .

## 3. Results and discussion

### 3.1. Basic properties of photocatalyst

Compared with NO, aromatic compounds with conjugated planar ring are more difficult to be decomposed [4]. Our early study found that In(OH)<sub>3</sub> (InOH) demonstrated a better behavior in degrading toluene and benzene than many reported photocatalysts [26]. Here, it is applied to control NO and toluene simultaneously, which are two representative compounds as both primary pollutants and the precursors for secondary atmospheric pollutants, like ozone [27]. The InOH catalyst shows a structure of nanosphere which is densely assembled from nanosheets as observed from SEM and TEM ([Fig. S3a–e](#)). The crystal structure of InOH is dominated by (200) as examined by XRD ([Fig. 2f](#)). The adsorption ability of catalyst for toluene was tested through gravity vacuum vapor sorption. P25 with a large surface area has been long considered as the most practical option for air purification application. As shown in [Fig. S4](#), the adsorption capacity of InOH is impressive, which is even three times higher than that of P25. A good adsorption ability to molecules like toluene, is a prerequisite for the sufficient degradation performance [28].

The chemical structure and optical property of the catalyst were investigated by XPS and UV-vis DRS ([Fig. S5a, b](#)). The band structure of InOH is depicted according to the valence band spectrum and Tauc plot (inner image of [Fig. S5b](#)). InOH is a typical wide-gap photocatalyst. The valence band position is negative enough to guarantee the generation of hydroxyl (·OH) and the conduction band position is positive enough to generate superoxide (·O<sub>2</sub>) radicals. The EPR recorded the rising signals of these reactive oxygen species with light irradiation ([Fig. S5c, d](#)). The reactive oxygen species act as the main oxidants in photocatalytic degradation of air pollutants.

### 3.2. Synergistic control of NO and C<sub>7</sub>H<sub>8</sub> and inhibition of O<sub>3</sub> generation

NO is the most common form of NO<sub>x</sub>, and toluene (C<sub>7</sub>H<sub>8</sub>) is one of the largest contribution VOCs to O<sub>3</sub> formation [29,30]. The photocatalytic degradation performance of mixed NO and C<sub>7</sub>H<sub>8</sub> was conducted in a continuous flow system. As a green technology operating under mild conditions, photocatalysis is suitable for treating low-concentration air pollutants to reach the ultra-low emission policy [31]. The initial total concentration of NO and C<sub>7</sub>H<sub>8</sub> is set to 60 ppm. The removal of pollutants at different mixing ratios (1:0, 3:1, 1:1, 1:3, 0:1) was examined first ([Fig. 1a](#)). Regardless of the mixing ratio, the total removal ratio of mixed pollutants is higher than that of a single pollutant. The maximum degradation is obtained at the mixing ratio of 1:1, and the photocatalyst has a stable performance ([Fig. 1b](#)). InOH shows no sign of inactivation after five hours of continuous testing. The total conversion efficiency of the mixed pollutants is up to 81.7%. More importantly, as NO and C<sub>7</sub>H<sub>8</sub> are the precursors for O<sub>3</sub> in photochemical reactions, the generation of O<sub>3</sub> in the blank system without photocatalyst and in the photocatalytic system with InOH photocatalyst has been detected by an ozone monitor. Over 360 ppb of O<sub>3</sub> is obviously generated in the blank system,

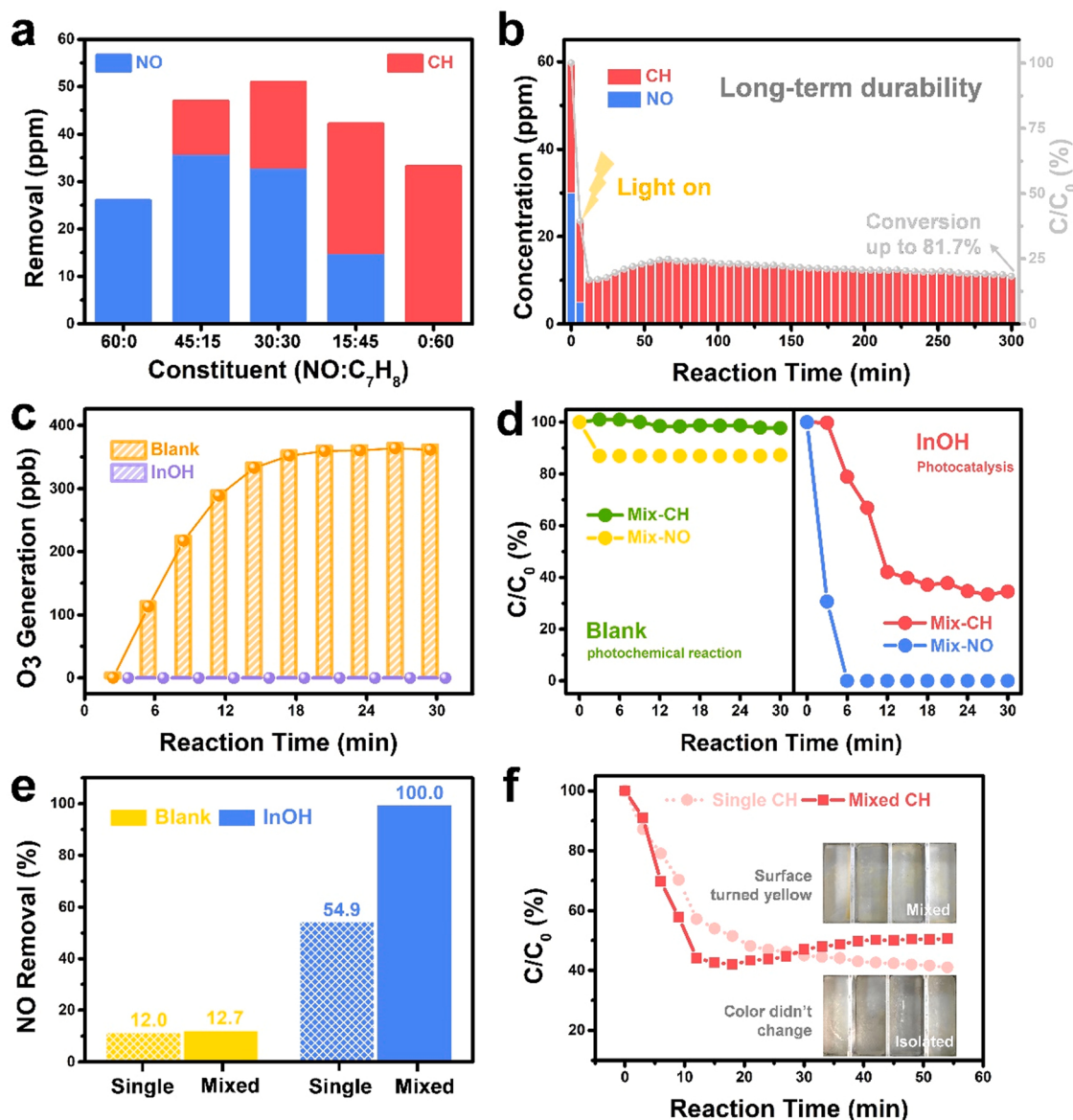


**Fig. 1.** (a) Photocatalytic performance: the removal of pollutants at different mixing ratios; (b) the long-term stability of the photocatalytic degradation of the mixture in the proportion of 1:1; (c) the generation of O<sub>3</sub> without and with photocatalyst under light irradiation; (d) the removal efficiency of mixed pollutants without and with photocatalyst; comparison of the photocatalytic degradation efficiency of (e) NO and (f) C<sub>7</sub>H<sub>8</sub> when they are isolated and mixed.

evidencing the photochemical reactions between NO and C<sub>7</sub>H<sub>8</sub> under light irradiation (Fig. 1c). Only 12.7% of NO and 2.2% of C<sub>7</sub>H<sub>8</sub> are converted in the blank system through photolysis and photochemical reaction (Fig. 1d). The control groups of O<sub>3</sub> generation during degradation of isolated pollutants were also conducted to support the results. Both in the blank or photocatalytic system, the O<sub>3</sub> generation in the control groups is neglectable (Fig. S6), indicating that the coexistence NO and C<sub>7</sub>H<sub>8</sub> is a necessity for photochemical O<sub>3</sub> production. In contrast to the blank system, no O<sub>3</sub> is detected during the photocatalytic degradation of NO and C<sub>7</sub>H<sub>8</sub> as shown in Fig. 1c, and the InOH photocatalyst exhibits high stability in inhibiting O<sub>3</sub> (Fig. S6).

Note that 100% of NO and 65.5% of C<sub>7</sub>H<sub>8</sub> are degraded by InOH photocatalyst when they coexist. In the blank system, the difference in removal efficiency of single NO and mixed NO is minor. Notably, compared to the removal of single NO, with the addition of C<sub>7</sub>H<sub>8</sub>, the photocatalytic removal efficiency of mixed NO is increased up to 100% (Fig. 1e). In the case of C<sub>7</sub>H<sub>8</sub>, as Fig. 1b shows, the degradation rate is slightly reduced in the first 60 min. So, the degradation performances of single C<sub>7</sub>H<sub>8</sub> and mixed C<sub>7</sub>H<sub>8</sub> in 60 min were compared. During the

degradation of mixed C<sub>7</sub>H<sub>8</sub>, the color of the photocatalyst turns yellow, while the photocatalyst remains white in the situation of degrading single C<sub>7</sub>H<sub>8</sub> (Fig. 1f). Compared to degradation of single C<sub>7</sub>H<sub>8</sub>, the degradation rate of mixed C<sub>7</sub>H<sub>8</sub> is fast at first and then becomes slowdown, which may be ascribed to the formation and ephemeral accumulation of intermediates. Nevertheless, the overall degradation ratios in 60 min in the two cases are similar, and the overall CO<sub>2</sub> selectivity is also close (84.5% and 81.4%). Mixing with NO does not affect the photocatalytic degradation of C<sub>7</sub>H<sub>8</sub>. The mechanism is further investigated in the later sections. In general, NO and C<sub>7</sub>H<sub>8</sub> exhibit a synergistic effect on the InOH photocatalyst during the mixed degradation process, especially for NO removal and O<sub>3</sub> inhibition.

### 3.3. Comparative adsorption of dual pollutants

Adsorption of reactants on catalyst surface has a great influence on the reaction. The comparative adsorption of NO and C<sub>7</sub>H<sub>8</sub> over the InOH photocatalyst was investigated first. We utilized *in situ* DRIFTS to explore the adsorption process on the catalyst surface in dark. Fig. 2a

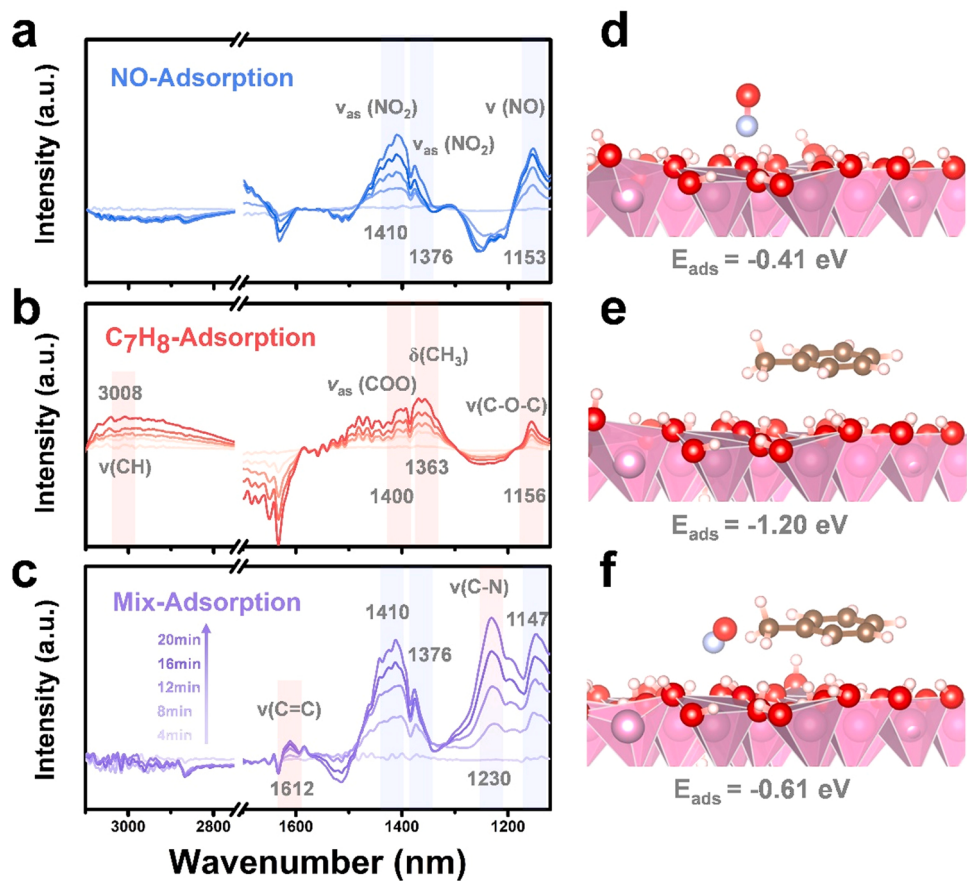


**Fig. 2.** Adsorption of reactants: *in situ* DRIFTS spectra for the adsorption of (a) NO, (b) C<sub>7</sub>H<sub>8</sub>, and (c) the mixture; adsorption energies of (d) single NO, (e) single C<sub>7</sub>H<sub>8</sub>, and (f) NO when C<sub>7</sub>H<sub>8</sub> is pre-adsorbed. Brown, grey, red, purple, and white spheres depict C, N, O, In, and H atoms, respectively.

records the adsorption processes for single NO. The IR signals of NO (1153 cm<sup>-1</sup>) and NO<sub>2</sub> (1410 and 1376 cm<sup>-1</sup>) gradually increase, [32, 33] suggesting that NO is adsorbed and partially oxidized. As shown in Fig. 2b, peaks at 3000 and 1363 cm<sup>-1</sup>, which could be assigned to the C-H stretching vibration of the aromatic ring [34]. The deformation vibration of the methyl group confirms the adsorption of toluene on the photocatalyst surface. Peaks at 1400 and 1156 cm<sup>-1</sup> assigned to COO and C-O-C species indicate the primary oxidation of C<sub>7</sub>H<sub>8</sub> on the catalyst [35,36]. The adsorption process of mixed NO and C<sub>7</sub>H<sub>8</sub> is further studied (Fig. 2c) when the dual pollutants were introduced into the reactor simultaneously. Instead of competitive sorption which was commonly reported among inorganic compounds, [37,38] the spectra show the signs of both C<sub>7</sub>H<sub>8</sub> and NO. The peak at 1612 cm<sup>-1</sup> can be assigned to the  $\nu(C=C)$  of the aromatic ring [39]. The peaks at 1410, 1376, and 1147 cm<sup>-1</sup> are related to NO, and the peaks of NO have a stronger response [32]. Besides, a unique IR signal at 1230 cm<sup>-1</sup> representing  $\nu(C-N)$  is observed [40]. The formed bond between the N atom in NO and the C atom in C<sub>7</sub>H<sub>8</sub> suggests the coupling reaction between C<sub>7</sub>H<sub>8</sub> and NO. Meanwhile, the peak ascribed to  $\nu(NO)$  shifts to the lower wavenumber. The weakening of the NO bond is supposed to be caused by the electron transfer between C<sub>7</sub>H<sub>8</sub> and NO in the coupling. The formation of coupling intermediate is considered to be responsible for the faster conversion rate of mixed C<sub>7</sub>H<sub>8</sub> than single C<sub>7</sub>H<sub>8</sub> in the early stage.

The mechanism of non-competitive adsorption was further studied by DFT calculation. The adsorption site and configuration of the single pollutant were optimized first. Two sites and two configurations for C<sub>7</sub>H<sub>8</sub>, and three sites and one configuration for NO were considered due to the surface structure and molecule coverage, as shown in Fig. S7. At the most stable adsorption site and configuration, the adsorption energies are calculated to be  $-0.41$  eV for NO and  $-1.20$  eV for C<sub>7</sub>H<sub>8</sub>.

(Fig. 2d, e). The adsorption of single C<sub>7</sub>H<sub>8</sub> on InOH photocatalyst is prior to NO, but the adsorption energy of NO is increased to  $-0.61$  eV when C<sub>7</sub>H<sub>8</sub> is pre-adsorbed on the photocatalyst (Fig. 2f). According to the configuration and DOS (Fig. S8), the pre-adsorbed C<sub>7</sub>H<sub>8</sub> can adjust the surface state of the InOH photocatalyst, enhancing the interaction between electrons on the  $\sigma^*_{1s}$  and  $\sigma_{2s}$  orbitals of NO and the surface. The introduction of NO to the pre-adsorbed surface lowers the energy of the whole system, explaining the non-competitive phenomenon observed in the *in situ* DRIFTS. The synergistic effect and coupling between NO and C<sub>7</sub>H<sub>8</sub> in the adsorption stage contribute directly to the photocatalytic degradation of mixed NO and C<sub>7</sub>H<sub>8</sub>, especially the conversion of NO.

### 3.4. Products distribution and in-depth mechanism for O<sub>3</sub> inhibition

To investigate the origin of the synergistic interaction between NO and C<sub>7</sub>H<sub>8</sub> in the photocatalytic degradation process, we utilized GCMS, IC, and *in situ* DRFTS to identify the key intermediates and products, tracing the conversion pathway of dual pollutants. The gas-phase intermediates in the outlet stream are collected and detected by GCMS (Table S1). Similar to the degradation of single toluene, [26] primary oxidation intermediates with the benzene ring, such as methyl phenol (C<sub>7</sub>H<sub>8</sub>O), benzaldehyde (C<sub>7</sub>H<sub>6</sub>O), and methyl benzoquinone (C<sub>7</sub>H<sub>6</sub>O<sub>2</sub>) are detected (Fig. 3a). As the degradation progresses, short chains intermediates after the opening of the ring, like butyl acetate (C<sub>6</sub>H<sub>12</sub>O<sub>2</sub>), ethylic acid (C<sub>2</sub>H<sub>4</sub>O<sub>2</sub>), and formic acid (CH<sub>2</sub>O) are generated. Typically, nitrotoluene (C<sub>7</sub>H<sub>7</sub>NO<sub>2</sub>) is detected. Nitrotoluene that consists of toluene bearing a nitro substituent is light yellow to yellow-brownish. The formation of nitrotoluene should be responsible for the color change of the photocatalyst during the degradation of mixed pollutants.

DFT calculation studied the charge density difference of toluene and

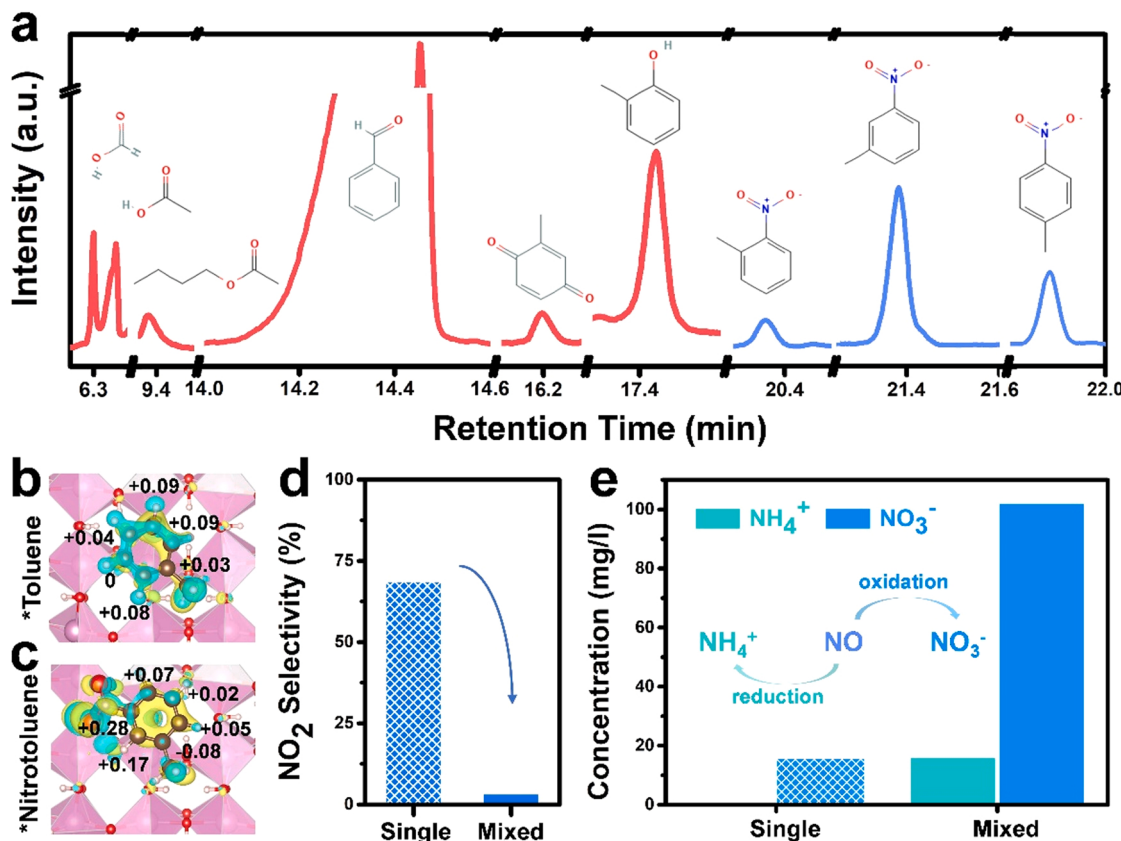


**Fig. 3.** Intermediates and products distribution: (a) GC-MS chromatogram of the outlet stream of photocatalytic degradation of the mixture; charge distribution of (b)  $\text{C}_7\text{H}_8$  and (c)  $\text{C}_7\text{H}_7\text{NO}_2$  on  $\text{In}(\text{OH})_3$  photocatalyst, blue and yellow clouds represent charge depletion and accumulation, and the isosurface level is set to  $0.0007 \text{ eV } \text{\AA}^{-3}$ ; (d)  $\text{NO}_2$  selectivity in photocatalytic degradation of single and mixed  $\text{NO}$ ; (e) the nitrogen-containing products identified by IC.

nitrotoluene on the  $\text{InOH}$  photocatalyst. As can be seen in Fig. 3b, when  $\text{C}_7\text{H}_8$  is adsorbed on the surface, the electron of the C atom at meta-position transfers to the surface, which makes meta-position an electron defect site.  $\text{NO}$  owns a lone pair electron [41]. An electron transfer trend between the defect site and  $\text{NO}$  would result in a coupling phenomenon. Thus, we can confirm the formation of the coupling intermediates ( $\text{C}_7\text{H}_7\text{NOH}$ ) observed in the adsorption process. Comparing Fig. 3b and c, the introduction of the nitro group changes the charge distribution of the benzene ring, breaking the equal distribution of electrons in the structure of  $\pi$ - $\pi$  stacking. Compared with toluene, the rearrangement of electrons makes it easier to open the ring for further mineralization. These intermediates are oxidized into nitrates,  $\text{CO}_2$ , and  $\text{H}_2\text{O}$  finally. So, although the formation of nitrotoluene slightly decreases the reaction rate in the early stage, the conversion efficiency and  $\text{CO}_2$  selectivity are not affected in the photocatalytic degradation of mixed pollutants. Nitrotoluene serves as a temporary and active intermediate.

In the photochemical reaction,  $\text{O}_3$  originates from the  $\text{O}^{(3)\text{P}}$  which is photolyzed from  $\text{NO}_2$  (R1–3). In the absence of VOC,  $\text{O}_3$  is consumed by  $\text{NO}$  in the oxidation to  $\text{NO}_2$  with no additional  $\text{O}_3$  accumulation. In the case of VOCs coexistence,  $\text{NO}$  tends to be oxidized to  $\text{NO}_2$  by organic peroxy radicals ( $\text{RO}_2$ ) rather than  $\text{O}_3$ , leading to net  $\text{O}_3$  production [13, 27, 42].



So, the transformation of nitrogen oxides is responsible for  $\text{O}_3$  accumulation, and  $\text{NO}_2$  as the direct precursor of  $\text{O}_3$  is the key

intermediate that should be avoided. In the reaction of mixed pollutants, the  $\text{NO}_2$  selectivity of the blank system is 31.4%, while that of the photocatalyst system is only 3.7% (Fig. S9). The high  $\text{NO}_x$  removal efficiency (high  $\text{NO}$  conversion and low  $\text{NO}_2$  selectivity) of  $\text{InOH}$  photocatalyst cuts off the generation path of  $\text{O}^{(3)\text{P}}$  and thus enables the almost complete inhibition of  $\text{O}_3$ . As shown in Fig. 3d, in the comparison of degradation of single and mixed pollutants, the low  $\text{NO}_2$  selectivity is contributed by the coexisting  $\text{C}_7\text{H}_8$ .

The products on the photocatalyst after reaction are washed and detected by IC (Fig. 3e). In the case of single  $\text{NO}$ ,  $\text{NO}$  is converted to  $\text{NO}_3^-$  besides  $\text{NO}_2$ . At the same time, both reduction and oxidation products are detected in the degradation of mixed  $\text{NO}$  and  $\text{C}_7\text{H}_8$ . The introduction of  $\text{C}_7\text{H}_8$  changes the conversion paths of  $\text{NO}$ . The production of nitrate is much more than that in the reaction of single  $\text{NO}$ , which can be ascribed to the coupling between  $\text{NO}$  and  $\text{C}_7\text{H}_8$ . Moreover, the protons and electrons that are released along the mineralization of  $\text{C}_7\text{H}_8$  enable the reduction of  $\text{NO}$ , resulting in the formation of  $\text{NH}_4^+$ . The changed reaction pathway greatly improves the conversion efficiency of  $\text{NO}$  (up to 100.0%) and decreases the  $\text{NO}_2$  selectivity (as low as 3.7%), which thus cuts off the generation path of  $\text{O}^{(3)\text{P}}$  and inhibits the formation of  $\text{O}_3$ .

According to the analysis of intermediates and products, the coupling between  $\text{NO}$  and  $\text{C}_7\text{H}_8$ , the  $\text{NO}$  oxidation to  $\text{NO}_2$  and the reduction to  $\text{NH}_4^+$  were simulated by DFT calculation. *O*-nitrotoluene, *m*-nitrotoluene, and *p*-nitrotoluene are all detected in the outlet stream, and the intensity of *m*-nitrotoluene is the strongest. The energies of these three isomers of nitrotoluene on the  $\text{InOH}$  photocatalyst were thereby calculated (Fig. S10). The configuration of *m*-nitrotoluene is the most stable, which supports the results of the highest intensity of *m*-nitrotoluene in the GCMS. So, the most possible coupling site for  $\text{NO}$  and  $\text{C}_7\text{H}_8$  is at the meta-position of  $\text{C}_7\text{H}_8$  to form the  $\text{C}_7\text{H}_7\text{NOH}$  intermediate in the adsorption. We calculated the Gibbs free energy for the first step of these

reactions (Fig. 4a). The negative value of free energy represents heat release. Among the three different conversion paths of NO, the  $\Delta G$  of oxidation is smaller ( $-0.38$  eV) than that of the reduction ( $-1.57$  eV) and coupling ( $-5.38$  eV). The result indicates the formation of  $\text{NO}_2$  on the  $\text{InOH}$  photocatalyst is less favorable than  $\text{NH}_4^+$  and  $\text{NO}_3^-$ . The coupling reaction resulting in the formation of  $\text{NO}_3^-$  is superior to the reduction reaction for the formation of  $\text{NH}_4^+$ . The competitive reactions revealed by DFT simulation explain the fact of low  $\text{NO}_2$  selectivity in the degradation of mixed pollutants on the  $\text{InOH}$  photocatalyst.

The reaction pathway of photocatalytic degradation of mixed NO and  $\text{C}_7\text{H}_8$  was explored by in situ DRIFTS (Fig. 4b). The IR signals at 3008 and 2881  $\text{cm}^{-1}$  belong to  $\nu(\text{C-H})$  of the aromatic ring and methyl group of  $\text{C}_7\text{H}_8$  [43,44]. The peak at 1147  $\text{cm}^{-1}$  belongs to NO. The signals of the reactants appear but do not increase with time, especially for NO [32]. The phenomenon is consistent with the trend in the removal efficiency evaluation. The bands at 1583 and 1405  $\text{cm}^{-1}$  can be assigned to the antisymmetric and symmetric stretching vibration of  $\text{COO}$ , and the bands at 1548  $\text{cm}^{-1}$  can be assigned to  $\nu(\text{C=O})$  [35,45]. These bonds can be ascribed to the organic aldehyde and acid intermediates, which agrees with the results of GCMS. Another obvious increasing peak at 1355  $\text{cm}^{-1}$  represents  $\nu(\text{NO}_2)$  of  $\text{Ar-NO}_2$  that belongs to nitrotoluene [40]. The bands at 1659 and 1642  $\text{cm}^{-1}$  can be assigned to  $\delta(\text{N-H})$ , [40] which can be attributed to intermediates formed during the reduction of NO.

### 3.5. Interaction between NO and $\text{C}_7\text{H}_8$ and reaction pathway

The overall reaction pathway is proposed in Fig. 5. When NO and  $\text{C}_7\text{H}_8$  coexist, we observe  $\text{O}_3$  accumulation under light irradiation through a series of photochemical reactions. NO is oxidized to  $\text{NO}_2$  by  $\text{RO}_2$  radicals, while the  $\text{NO}_2$  will be further photolyzed into NO and O

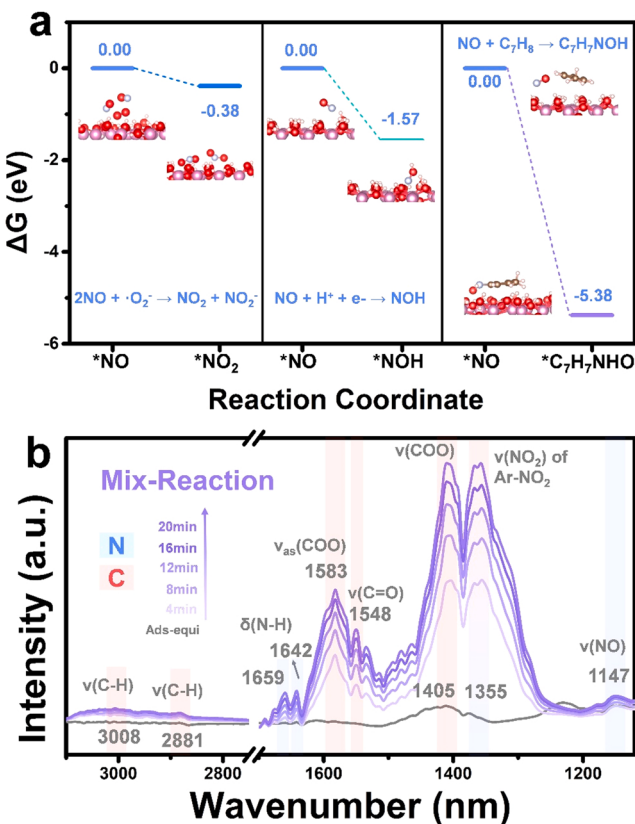


Fig. 4. Reaction pathway: (a) the Gibbs free energy of NO conversion through different reaction paths; (b) in situ DRIFTS spectra for the photocatalytic reaction of NO and  $\text{C}_7\text{H}_8$ .

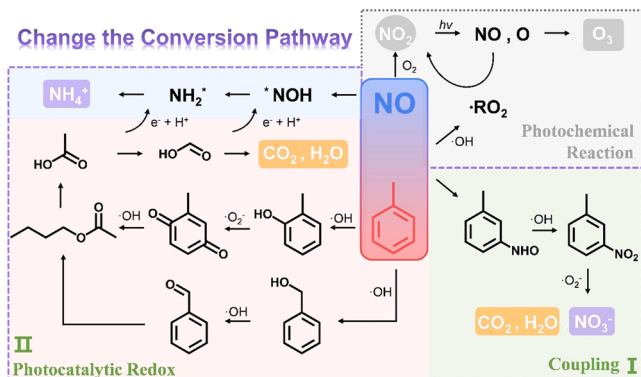


Fig. 5. Schematic illustration of conversion pathway for synergistic control of primary (NO and  $\text{C}_7\text{H}_8$ ) and secondary ( $\text{O}_3$ ) pollutants.

( $^3\text{P}$ ).  $\text{O}({}^3\text{P})$  combines with  $\text{O}_2$  to form  $\text{O}_3$ , and NO will be oxidized to  $\text{NO}_2$  again by  $\cdot\text{RO}_2$  converted from  $\text{C}_7\text{H}_8$ . Thus, the cycle leads to a net  $\text{O}_3$  accumulation. The  $\text{InOH}$  photocatalyst will change the reaction pathway between NO and  $\text{C}_7\text{H}_8$  and avoid the formation of  $\text{NO}_2$  which is the direct precursor of  $\text{O}_3$ . On the  $\text{InOH}$  photocatalyst, NO will couple with  $\text{C}_7\text{H}_8$  at the meta-position in the adsorption stage. The formed  $\text{C}_7\text{H}_2\text{NOH}$  will be oxidized to  $\text{C}_7\text{H}_6\text{NO}_2$  and finally decomposed into  $\text{NO}_3^-$  (accumulated on the catalyst),  $\text{CO}_2$ , and  $\text{H}_2\text{O}$  in the photocatalytic reaction (Fig. S11). On the other hand,  $\text{C}_7\text{H}_8$  itself can be first oxidized to phenol, benzaldehyde, benzoquinone, et al. Then the benzene ring is open and decomposed into small molecules like butyl acetate, ethylic acid,  $\text{CO}_2$ , and  $\text{H}_2\text{O}$ . The band structure of  $\text{InOH}$  photocatalyst allows the reduction reaction. The protons and electrons released in the mineralization of  $\text{C}_7\text{H}_8$  can directly reduce NO to  $\text{NH}_4^+$ . The photocatalytic coupling and redox reactions between NO and  $\text{C}_7\text{H}_8$  suppress the generation of  $\text{NO}_2$  and thus inhibit the formation of  $\text{O}_3$ .

### 4. Conclusion

The coexistence of multiple pollutants is normal in actual scenarios, but few studies have considered the degradation of multiple pollutants due to the complexity of the reaction processes and the limitation of the analysis methods.  $\text{NO}_x$  and VOCs are not only primary pollutants and will also cause secondary pollutants like  $\text{O}_3$  through photochemical reactions. Photocatalysis technology utilizing sunlight could turn predicament into power, change the reaction pathway between  $\text{NO}_x$  and VOCs and serve as a green and efficient method to synergistically control multiple pollutants. For the first time, we investigate the photocatalytic degradation of mixed NO and  $\text{C}_7\text{H}_8$  for inhibition of photochemical  $\text{O}_3$  production on  $\text{In(OH)}_3$ . This synergistic effect originates from the changed reaction path of NO brought by the coexistence of  $\text{C}_7\text{H}_8$ . The protons and electrons released during the mineralization of  $\text{C}_7\text{H}_8$  can reduce NO to  $\text{NH}_4^+$ . The coupling and reduction reactions are more favorable than the oxidation of NO to  $\text{NO}_2$ , accounting for the enhanced NO removal and  $\text{O}_3$  inhibition. This work achieves the simultaneous and synergistic control of NO, VOC and  $\text{O}_3$  by photocatalysis. These findings pave the way for application of photocatalytic control of multi pollutants and deepen the mechanistic understanding of degradation of mixed pollutants.

### CRediT authorship contribution statement

**Kanglu Li:** Data curation, Formal analysis, Methodology, Visualization, Writing – original draft. **Hong Wang:** Formal analysis, Methodology, Visualization. **Lvcun Chen:** Formal analysis, Methodology. **Jieyuan Li:** Data curation, Methodology. **Fan Dong:** Conceptualization, Funding acquisition, Supervision, Writing – review & editing.

## Declaration of Competing Interest

The authors declare that they have no known competing financial interests or personal relationships that could have appeared to influence the work reported in this paper.

## Acknowledgments

This work was supported by the National Natural Science Foundation of China (Grant Nos. 22176029, 21822601), the Sichuan Natural Science Foundation for Distinguished Scholars (2021JDJQ0006), the Fundamental Research Funds for the Central Universities (ZYGX2019Z021) and the Sichuan Science and Technology Program (No. 2022JDRC0084).

## Supplementary material

Details of characterization, experimental setup, SEM images, TEM images, XRD pattern, adsorption capacity-time curve, XPS spectrum, UV-vis DRS spectra, EPR spectra, O<sub>3</sub> suppression stability and control group, adsorption optimization, DOS, identified intermediates, NO<sub>2</sub> selectivity, nitrotoluene isomers, CO<sub>2</sub> production.

## Appendix A. Supporting information

Supplementary data associated with this article can be found in the online version at [doi:10.1016/j.apcatb.2022.121423](https://doi.org/10.1016/j.apcatb.2022.121423).

## References

- [1] S. Chen, H. Wang, M. Shi, H. Ye, Z. Wu, Deep oxidation of NO by a hybrid system of plasma-N-type semiconductors: high-energy electron-activated “pseudo photocatalysis” behavior, *Environ. Sci. Technol.* 52 (2018) 8568–8577.
- [2] H. Wang, K. Li, J. Li, Y. Sun, F. Dong, Photochemical transformation pathways of nitrates from photocatalytic NO<sub>x</sub> oxidation: implication for controlling secondary pollutant, *Environ. Sci. Technol. Lett.* 8 (2021) 873–877.
- [3] W. Zhang, Y. Wang, Y. Wang, Y. Liang, F. Dong, Highly efficient photocatalytic NO removal and in situ DRIFTS investigation on SrSn(OH)<sub>6</sub>, *Chin. Chem. Lett.* 33 (2022) 1259–1262.
- [4] W. Qu, P. Wang, M. Gao, J.Y. Hasegawa, Z. Shen, Q. Wang, R. Li, D. Zhang, Delocalization effect promoted the indoor air purification via directly unlocking the ring-opening pathway of toluene, *Environ. Sci. Technol.* 54 (2020) 9693–9701.
- [5] M. Xu, Y. Chen, J. Qin, Y. Feng, W. Li, W. Chen, J. Zhu, H. Li, Z. Bian, Unveiling the role of defects on oxygen activation and photodegradation of organic pollutants, *Environ. Sci. Technol.* 52 (2018) 13879–13886.
- [6] C. He, Y. Wang, Z. Li, Y. Huang, Y. Liao, D. Xia, S. Lee, Facet engineered alpha-MnO<sub>2</sub> for efficient catalytic ozonation of odor CH<sub>3</sub>SH: oxygen vacancy-induced active centers and catalytic mechanism, *Environ. Sci. Technol.* 54 (2020) 12771–12783.
- [7] A. Mellouki, T.J. Wallington, J. Chen, Atmospheric chemistry of oxygenated volatile organic compounds: impacts on air quality and climate, *Chem. Rev.* 115 (2015) 3984–4014.
- [8] Z. Meng, D. Dabdub, J.H. Seinfeld, Chemical coupling between atmospheric ozone and particulate matter, *Science* 277 (1997) 116–119.
- [9] Q. Zhang, Y. Shi, X. Shi, T. Huang, S. Lee, Y. Huang, J.J. Cao, Constructing Pd/ferroelectric Bi<sub>4</sub>Ti<sub>3</sub>O<sub>12</sub> nanoflake interfaces for O<sub>2</sub> activation and boosting NO photo-oxidation, *Appl. Catal. B: Environ.* 302 (2022), 120876.
- [10] Y. Xie, H. Dai, Y. Zhang, Y. Wu, T. Hanaoka, T. Masui, Comparison of health and economic impacts of PM2.5 and ozone pollution in China, *Environ. Int.* 130 (2019), 104881.
- [11] K. Li, D.J. Jacob, H. Liao, L. Shen, Q. Zhang, K.H. Bates, Anthropogenic drivers of 2013–2017 trends in summer surface ozone in China, *Proc. Natl. Acad. Sci. USA* 116 (2019) 422–427.
- [12] R. Wu, S. Xie, Spatial distribution of ozone formation in China derived from emissions of speciated volatile organic compounds, *Environ. Sci. Technol.* 51 (2017) 2574–2583.
- [13] K. Lu, S. Guo, Z. Tan, H. Wang, D. Shang, Y. Liu, X. Li, Z. Wu, M. Hu, Y. Zhang, Exploring atmospheric free-radical chemistry in China: the self-cleansing capacity and the formation of secondary air pollution, *Natl. Sci. Rev.* 6 (2019) 579–594.
- [14] K. Li, D.J. Jacob, H. Liao, J. Zhu, V. Shah, L. Shen, K.H. Bates, Q. Zhang, S. Zhai, A two-pollutant strategy for improving ozone and particulate air quality in China, *Nat. Geosci.* 12 (2019) 906–910.
- [15] D. Ding, J. Xing, S. Wang, Z. Dong, F. Zhang, S. Liu, J. Hao, Optimization of a NO<sub>x</sub> and VOC cooperative control strategy based on clean air benefits, *Environ. Sci. Technol.* 56 (2022) 739–749.
- [16] F. He, W. Jeon, W. Choi, Photocatalytic air purification mimicking the self-cleaning process of the atmosphere, *Nat. Commun.* 12 (2021) 2528.
- [17] J. Qu, D. Chen, N. Li, Q. Xu, H. Li, J. He, J. Lu, Ternary photocatalyst of atomic-scale Pt coupled with MoS<sub>2</sub> co-loaded on TiO<sub>2</sub> surface for highly efficient degradation of gaseous toluene, *Appl. Catal. B: Environ.* 256 (2019), 117877.
- [18] G. Dong, L. Zhao, X. Wu, M. Zhu, F. Wang, Photocatalysis removing of NO based on modified carbon nitride: the effect of celestite mineral particles, *Appl. Catal. B: Environ.* 245 (2019) 459–468.
- [19] H. Shang, M. Li, H. Li, S. Huang, C. Mao, Z. Ai, L. Zhang, Oxygen vacancies promoted the selective photocatalytic removal of NO with Blue TiO<sub>2</sub> via simultaneous molecular oxygen activation and photogenerated hole annihilation, *Environ. Sci. Technol.* 53 (2019) 6444–6453.
- [20] H. Wang, X. Dong, R. Tang, J. Li, Y. Sun, Z. Wang, K.-H. Kim, F. Dong, Selective breakage of C-H bonds in the key oxidation intermediates of gaseous formaldehyde on self-doped CaSn(OH)<sub>6</sub> cubes for safe and efficient photocatalysis, *Appl. Catal. B: Environ.* 277 (2020), 119214.
- [21] Q. Liu, W. Zhao, Z. Ao, T. An, Photo-piezoelectric synergistic degradation of typical volatile organic compounds on BaTiO<sub>3</sub>, *Chin. Chem. Lett.* 33 (2022) 410–414.
- [22] B. Wang, Z. Song, L. Sun, A review: comparison of multi-air-pollutant removal by advanced oxidation processes – industrial implementation for catalytic oxidation processes, *Chem. Eng. J.* 409 (2021), 128136.
- [23] B. Yuan, X. Mao, Z. Wang, R. Hao, Y. Zhao, Radical-induced oxidation removal of multi-air-pollutant: a critical review, *J. Hazard. Mater.* 383 (2020), 121162.
- [24] A. Mahmood, X. Wang, X. Xie, J. Sun, Degradation behavior of mixed and isolated aromatic ring containing VOCs: Langmuir–Hinselwood kinetics, photodegradation, in-situ FTIR and DFT studies, *J. Environ. Chem. Eng.* 9 (2021), 105069.
- [25] C. Yan, L. Liu, Oxidation of gas phase ammonia via accelerated generation of radical species and synergy of photo electrochemical catalysis with persulfate activation by CuO–Co<sub>3</sub>O<sub>4</sub> on cathode electrode, *J. Hazard. Mater.* 388 (2020), 121793.
- [26] K. Li, Y. He, J. Li, J. Sheng, Y. Sun, J. Li, F. Dong, Identification of deactivation-resistant origin of In(OH)<sub>3</sub> for efficient and durable photodegradation of benzene, toluene and their mixtures, *J. Hazard. Mater.* 416 (2021), 126208.
- [27] W.L. Chameides, F. Fehsenfeld, M.O. Rodgers, C. Cardelino, J. Martinez, D. Parrish, W. Lonneman, D.R. Lawson, R.A. Rasmussen, P. Zimmerman, J. Greenberg, P. Middleton, T. Wang, Ozone precursor relationships in the ambient atmosphere, *J. Geophys. Res.* 97 (1992) 6037.
- [28] D. Liu, D. Chen, N. Li, Q. Xu, H. Li, J. He, J. Lu, ZIF-67-Derived 3D hollow mesoporous crystalline Co<sub>3</sub>O<sub>4</sub> wrapped by 2D g-C<sub>3</sub>N<sub>4</sub> nanosheets for photocatalytic removal of nitric oxide, *Small* 15 (2019), e1902291.
- [29] X.Y. Wu, K.K. Zhang, G.K. Zhang, S. Yin, Facile preparation of BiOX (X = Cl, Br, I) nanoparticles and up-conversion phosphors/BiOBr composites for efficient degradation of NO gas: oxygen vacancy effect and near infrared light responsive mechanism, *Chem. Eng. J.* 325 (2017) 59–70.
- [30] H. Schwartz-Narbonne, S.H. Jones, D.J. Donaldson, Indoor lighting releases gas phase nitrogen oxides from indoor painted surfaces, *Environ. Sci. Technol. Lett.* 6 (2019) 92–97.
- [31] F. He, S. Weon, W. Jeon, M.W. Chung, W. Choi, Self-wetting triphase photocatalysis for effective and selective removal of hydrophilic volatile organic compounds in air, *Nat. Commun.* 12 (2021) 6259.
- [32] K.I. Hadjiivanov, Identification of neutral and charged N<sub>x</sub>O<sub>y</sub> surface species by IR spectroscopy, *Catal. Rev.* 42 (2000) 71–144.
- [33] M.A. Debeila, N.J. Coville, M.S. Scurrell, G.R. Hearne, The effect of calcination temperature on the adsorption of nitric oxide on Au-TiO<sub>2</sub>: drifts studies, *Appl. Catal. A: Gen.* 291 (2005) 98–115.
- [34] M.D. Hernández-Alonso, I. Tejedor-Tejedor, J.M. Coronado, M.A. Anderson, Operando FTIR study of the photocatalytic oxidation of methylcyclohexane and toluene in air over TiO<sub>2</sub>–ZrO<sub>2</sub> thin films: influence of the aromaticity of the target molecule on deactivation, *Appl. Catal. B: Environ.* 101 (2011) 283–293.
- [35] Y. He, Z. Rui, H. Ji, In situ DRIFTS study on the catalytic oxidation of toluene over V<sub>2</sub>O<sub>5</sub>/TiO<sub>2</sub> under mild conditions, *Catal. Commun.* 14 (2011) 77–81.
- [36] S. Mo, Q. Zhang, M. Zhang, Q. Zhang, J. Li, M. Fu, J. Wu, P. Chen, D. Ye, Elucidating the special role of strong metal–support interactions in Pt/MnO<sub>2</sub> catalysts for total toluene oxidation, *Nanoscale Horiz.* 4 (2019) 1425–1433.
- [37] Z. Lin, W. Shen, J.C. Roux, H. Xi, Photo-catalytic degradation of mixed gaseous HCHO and C<sub>6</sub>H<sub>6</sub> in paper mills: experimental and theoretical study on the adsorption behavior simulation and catalytic reaction mechanism, *J. Hazard. Mater.* 388 (2020), 121779.
- [38] Z. Chen, H. Yin, C. Wang, R. Wang, Y. Peng, C. You, J. Li, New insights on competitive adsorption of NO/SO<sub>2</sub> on TiO<sub>2</sub> anatase for photocatalytic NO oxidation, *Environ. Sci. Technol.* 55 (2021) 9285–9292.
- [39] X. Li, X. Zou, Z. Qu, Q. Zhao, L. Wang, Photocatalytic degradation of gaseous toluene over Ag-doping TiO<sub>2</sub> nanotube powder prepared by anodization coupled with impregnation method, *Chemosphere* 83 (2011) 674–679.
- [40] W.W. Simons, The Sadtler handbook of infrared spectra, Sadtler Research Laboratories, Philadelphia, 1978.
- [41] G. Dong, W. Ho, Y. Li, L. Zhang, Facile synthesis of porous graphene-like carbon nitride (C<sub>6</sub>N<sub>9</sub>H<sub>3</sub>) with excellent photocatalytic activity for NO removal, *Appl. Catal. B: Environ.* 174–175 (2015) 477–485.
- [42] Y. Fang, L. Li, J. Yang, S. Hoang, L. Wang, J. Xu, W. Yang, C. Pan, Y. Zhu, H. Deng, Z. Luo, C. Sun, D. Gao, Z. Li, Y. Guo, Engineering the nucleophilic active oxygen species in CuTiO<sub>x</sub> for efficient low-temperature propene combustion, *Environ. Sci. Technol.* 54 (2020) 15476–15488.

[43] R.M. Serra, E.E. Miró, A.V. Boix, FTIR study of toluene adsorption on Cs-exchanged mordenites, *Microporous Mesoporous Mater.* 127 (2010) 182–189.

[44] A.J. Maira, J.M. Coronado, V. Augugliaro, K.L. Yeung, J.C. Conesa, J. Soria, Fourier transform infrared study of the performance of nanostructured TiO<sub>2</sub> particles for the photocatalytic oxidation of gaseous toluene, *J. Catal.* 202 (2001) 413–420.

[45] X. Zou, C. Yuan, Y. Dong, H. Ge, J. Ke, Y. Cui, Lanthanum orthovanadate/bismuth oxybromide heterojunction for enhanced photocatalytic air purification and mechanism exploration, *Chem. Eng. J.* 379 (2020), 122380.